Analysis of nuclear properties of symmetry breaking pear-shaped nuclei in relation with CP-violating effects

Department of Physics

Supervisor:
Gillis Carlsson
Division of Mathematical Physics, Lund

Author:
Zi Yao Lim

General Physics Bachelor's Thesis, 15hp

Examination: May 2024

List of Abbreviations

$\mathcal{P}$	Parity
$\mathcal{T}$	Time
BCS	Bardeen–Cooper–Schrieffer
EDM	Electric Dipole Moment
EXP.	Exprerimental data
Fig.	Figure
HF	Hartree-Fock
HFBTHOv2	HFBTHO v2.00d code
HFBTHOv4	HFBTHO v4.0 code
Osc.	Oscillator
Quasi-Particle	Q.p
Ra	Radium
The.	Theory
SkyAx	SkyAx code

Abstract

To investigate the non-zero nuclear Schiff moment exhibited by $\mathcal{PT}$-violating nuclei, this paper examines the prediction of shapes and excited states of Radium isotopes by applying different Skyrme-like models. The calculations were conducted by employing computational programs incorporating both the Hartree-Fock-Bogoliubov method and Hartree-Fock + BCS with an effective Skyrme force. A preliminary survey of nuclear properties that contribute to the enhancement of the nuclear Schiff moment is also presented.

The content, findings and text of the thesis are results of my work. Syntax and grammar of the text have been polished with the aid of ChatGPT.

Contents

1 Introduction

Measuring the electric dipole moment (EDM) of atoms stands out as one of the most promising ways to investigate $\mathcal{CP}$-violation and is actively pursued by numerous ongoing research efforts. The electric dipole moment EDM refers to the separation of positive and negative charge within the atom along its angular momentum axis [1]. It is known that this dipole moment is virtually fully screened by the constituent atomic electrons.

However, a component known as the nuclear Schiff moment is responsible for inducing a non-zero permanent atomic EDM when both parity ($\mathcal{P}$) and time reversal ($\mathcal{T}$) are simultaneously violated [2], indicating the presence of $\mathcal{CP}$-violating forces. This nuclear Schiff moment is extremely sensitive to $\mathcal{PT}$-violation, making it a prime candidate for this study.

The expectation of the nuclear Schiff moment $\langle \mathbf{S} \rangle$ can be evaluated using perturbation theory since it is induced by a very weak $\mathcal{PT}$-violating interaction $\hat{V}_{\mathcal{PT}}$,

$$\langle \mathbf{S} \rangle = \sum_{n>0} \frac{\langle \Psi_0 | \hat{\mathbf{S}}_Z | \Psi_n \rangle \langle \Psi_n | \hat{V}_{\mathcal{PT}} | \Psi_0 \rangle}{E_0 - E_n} \approx \frac{1}{\Delta E} \langle \Psi_0 | \hat{\mathbf{S}}_Z | \Psi_1 \rangle \langle \Psi_1 | \hat{V}_{\mathcal{PT}} | \Psi_0 \rangle. \tag{1}$$

Where, $\hat{\mathbf{S}}_Z$ denotes the Schiff moment operator along the symmetry axis (Z-axis), $|\Psi_n\rangle$ are excited opposite parity states of the ground state $|\Psi_0\rangle$, with the condition that $I \neq 0$. This expression can then be simplified further by only considering the first excited state $|\Psi_1\rangle$, which exhibit the smallest energy difference $\Delta E = E_0 - E_n$ compared to the energy E_0 from $|\Psi_0\rangle$. In the absence of $\hat{V}_{\mathcal{PT}}$, $\langle \mathbf{S} \rangle$ will always be zero.

Furthermore, the magnitude of the nuclear Schiff moment is highly amplified in specific deformed nuclear shapes. Deformed nuclei refer to nuclei that exhibit non-spherical shapes, arising from uneven nucleon density distribution caused by the collective motion of nucleons within the nucleus. Octupole and quadrupole moments are empirical quantities which can be measured from experiments to quantify the deformity of these nuclei. Quadrupole deformed nuclei typically resemble either a prolate ellipsoid or an oblate ellipsoid. On the other hand, octupole deformed nuclei often exhibit a pear-like shape and are commonly known as pear-shaped nuclei.

Pear-shaped nuclei are known to exhibit spontaneous $\mathcal{P}$-violation due to their assymetrical shape under reflection. Studies have shown that the restoration of this symmetry leads to the formation of parity doublets within these nuclei, particularly in odd mass nuclei [3, 4, 5]. Parity doublets are observed as rotational band heads with nearly degenerate states of opposite parity but the same spin, resulting in an enhanced nuclear Schiff moment. This makes odd mass pear-shaped nuclei valuable candidates for this study, especially Radium isotopes, Ra223 and 225 with very close-lying parity doublet seperation ΔE of $\approx$ 50keV [3, 6].

Our study focuses on the aforementioned features which enhance the nuclear Schiff moment, by mainly employing the Hartree-Fock-Bogoliubov (HFB) method. This approach

allows us to compare the predictions of shapes and excited states between different theoretical models and its relation with the nuclear Schiff moment.

2 Background Theory

2.1 Hartree-Fock (HF)

The Hartree-Fock (HF) Theory applies the variational approach to solve for a single-particle potential from two-body interactions until a self-consistent mean field is obtained. It is based upon the assumption that each nucleon moves independently in a mean field potential induced by all other nucleons in the system. This is justified phenomenologically by the nuclear shell model [7]; the nucleons are described in terms of orbitals and shells with discrete energy levels, analogous to the shell structure of electrons in atoms.

An example Hamiltonian acting on a many-body system may be expressed as [8]:

$$\hat{H} = \sum_{i=1}^{A} \hat{t}_i + \frac{1}{2} \sum_{i \neq j}^{A} v(\mathbf{r}_i, \mathbf{r}_j), \tag{2}$$

where $\hat{H}$ represents the Hamiltonian operator, $\hat{t}_i$ denotes the kinetic energy operator for the i-th particle, $v(\mathbf{r}_i, \mathbf{r}_j)$ represents the two-body interaction depending on the particles' positions $\mathbf{r}_i$, $\mathbf{r}_j$ and A is the total number of particles in the system.

In the HF approximation, the many-body problem of Eq. 2 is simplified by introducing an average single-particle potential, often referred to as the HF potential. This potential accounts for the mean field experienced by each particle due to the presence of all other particles in the system. This approximation leades to a single-particle Schrödinger-like equation [7]:

$$\hat{h} = \sum_{i=1}^{A} \hat{h}_i \ ; \ \hat{h}_i = \hat{t}_i + v(\mathbf{r}_i), \tag{3}$$

The sum of the one-body Hamiltonian operators $\hat{h}$ can be derived and follows from assuming a a Slater Determinant $\Phi_A(\mathbf{r}_1, \mathbf{r}_2, \ldots, \mathbf{r}_A)$ as the trial wave function (see Appendix A). The goal is to find the eigenfunction corresponding to the lowest energy E_0, which approximates the exact ground state determined through the variational approach.

The expectation value of the Hamiltonian can be written in terms of the Slater determinant as:

$$E = \langle \Phi_A | \hat{H} | \Phi_A \rangle \tag{4}$$

$$= \sum_{i=1}^{A} \langle i | \hat{t}_i | i \rangle + \frac{1}{2} \sum_{i,j}^{A} \left[\langle ij | \hat{V} | ij \rangle - \langle ij | \hat{V} | ji \rangle \right]^{1} \tag{5}$$

with $\langle ij|\hat{V}|kl\rangle = \iint d\mathbf{r}_1\, d\mathbf{r}_2\, \phi_i^*(\mathbf{r}_1)\phi_j^*(\mathbf{r}_2)v(\mathbf{r}_1,\mathbf{r}_2)\phi_k(\mathbf{r}_1)\phi_l(\mathbf{r}_2)$. Since fermions are indistinguishable, it is implied that the interaction is symmetric with respect to change of coordinates which results in the symmetry of $\langle ij|\hat{V}|kl\rangle = \langle ji|\hat{V}|lk\rangle$.

The variational method involves optimising the single-particle orbitals $\{\phi_k\}_{k=1,\cdots,A}$. This is done by minimising the energy functional E with respect to ϕ_k. This optimization process seeks to find the single-particle orbitals that collectively minimize the energy functional. The solution is obtained when

$$\delta E = \frac{\langle\Phi_A|\hat{H}|\Phi_A\rangle}{\langle\Phi_A|\Phi_A\rangle} = \delta\left[\langle\Phi_A|\hat{H}|\Phi_A\rangle - \sum_i^A \epsilon_i \int d\mathbf{r}\,|\phi_i|^2\right] = 0$$

ϵ_i is the Lagrange multiplier that serves as a constraint to preserve the norm of each state ($\int d\mathbf{r}|\phi_i|^2 = 1$) during the variation process.

Since $|\Phi_A\rangle$ is complex, the real and imaginary part can be treated independently. Solving the functional derivative E with respect to ϕ_i or ϕ_i^* yields equivalent result as the Hamiltonian is hermitian.

Perfoming the variational approach to the kinetic energy term with respect to ϕ_k^* yields:

$$\begin{aligned}\delta\sum_{i=1}^A\langle i|\hat{t}_i|i\rangle &= \int \frac{\partial}{\partial\phi_k^*}\left[\phi_i^*\hat{t}\phi_i\right]\delta\phi_k^*\mathbf{r}\\ &= \int \hat{t}\phi_k\delta\phi_k^* d\mathbf{r},\end{aligned}$$

and for the first term in the potential shows:

$$\delta\sum_{i,j}^A\langle ij|\hat{V}|ij\rangle = \int d\mathbf{r_1}\int d\mathbf{r_2}\left[\sum_{i,j}^A \phi_j^*(\mathbf{r_2})v(\mathbf{r_1},\mathbf{r_2})\phi_k(\mathbf{r_1})\phi_j(\mathbf{r_2})\right]\delta\phi_k^*(\mathbf{r_1})\delta_{i,k} \tag{6}$$

$$+\int d\mathbf{r_1}\int d\mathbf{r_2}\left[\sum_{i,j}^A \phi_i^*(\mathbf{r_1})v(\mathbf{r_1},\mathbf{r_2})\phi_i(\mathbf{r_1})\phi_k(\mathbf{r_2})\right]\delta\phi_k^*(\mathbf{r_2})\delta_{j,k} \tag{7}$$

$$= 2\int d\mathbf{r_1}\int d\mathbf{r_2}\left[\sum_{j}^A \phi_j^*(\mathbf{r_2})v(\mathbf{r_1},\mathbf{r_2})\phi_j(\mathbf{r_2})\right]\phi_k(\mathbf{r_1})\delta\phi_k^*(\mathbf{r_1}). \tag{8}$$

where $\delta_{a,b}$ is the Kronecker delta, defined as $\delta_{a,b} = \begin{cases}1, & \text{if } a = b\\ 0, & \text{if } a \neq b\end{cases}$.

From the Born interpretation, the probability density of finding a particle at a given point in space is given by the square of the magnitude of the wavefunction associated with that

[1]In Eq .5, the term $\langle ij|\hat{V}|ij\rangle$ suggests that interaction between two fermions in the same quantum state $i = j$ is possible. However, due to the inherent antisymmetry of the wave functions in the Slater determinant, this term vanishes upon calculation. This ensure that Pauli exclusion obeyed, where no two fermions can occupy the same quantum state simultaneously.

particle. Thus, the particle density for a system with A particles is $\sum_i^A |\phi_i(\mathbf{r})|^2 = \rho(\mathbf{r})$.It is noted that the integration of particle density results in the total number of particles $\int \rho(\mathbf{r}) d\mathbf{r} = A$. Expressing Eq. 8 in terms of $\rho(\mathbf{r})$ yields

$$\delta \sum_{i,j}^{A} \langle ij|\hat{V}|ij\rangle = 2 \int d\mathbf{r_1} V_H(\mathbf{r_1}) \phi_k(\mathbf{r_1}) \delta\phi_k^*(\mathbf{r_1}),$$

with the Hartree potential denoted as $V_H(\mathbf{r_1}) = \int d\mathbf{r_2} v(\mathbf{r_1}, \mathbf{r_2}) \rho(\mathbf{r_2})$.

Upon closer inspection, one would notice that the potential of a particle at $\mathbf{r_1}$ due to interactions with other particles are described by ρ. Since ρ also includes the contribution of the particle at $\mathbf{r_1}$, this would mean that the potential includes interaction of the particle with itself (self-interaction), which is un-physical. This discrepancy is accounted for in the latter potential term in Eq. 5.

Performing the variational method to the latter potential term leads to

$$\delta \sum_{i,j}^{A} \langle ij|\hat{V}|ji\rangle = 2 \int d\mathbf{r_1} \int d\mathbf{r_2} \left[\sum_{j}^{A} \phi_j^*(\mathbf{r_2}) v(\mathbf{r_1}, \mathbf{r_2}) \phi_j(\mathbf{r_1}) \right] \phi_k(\mathbf{r_2}) \delta\phi_k^*(\mathbf{r_1}).$$

By introducing a non-local density term, $\sum_j^A \phi_j^*(\mathbf{r}_2)\phi_j(\mathbf{r}_1) = \rho(\mathbf{r}_1, \mathbf{r}_2)$, the equation simplifies to

$$-\frac{1}{2}\delta \sum_{i,j}^{A} \langle ij|\hat{V}|ji\rangle = \int d\mathbf{r}_1 \int d\mathbf{r}_2 V_F(\mathbf{r}_1, \mathbf{r}_2) \phi_k(\mathbf{r}_2) \delta\phi_k^*(\mathbf{r}_1).$$

where the Fock potential is expressed as $V_F(\mathbf{r}_1, \mathbf{r}_2) = -v(\mathbf{r}_1, \mathbf{r}_2)\rho(\mathbf{r}_1, \mathbf{r}_2)$.

By introducing the Fock operator $\hat{V}_F \phi_k(\mathbf{r}) = \int V_F(\mathbf{r}, \mathbf{r}')\phi_k(\mathbf{r}')d\mathbf{r}'$, the final expression is obtained whereby the orbital is an eigenfunction of the Hamiltonian operator:

$$\left[\hat{t} + V_H + \hat{V}_F\right] \phi_k(\mathbf{r}') = \epsilon_k \phi_k(\mathbf{r}').$$

The Hartree potential V_H can be interpreted as a mean potential induced and experienced by all particles in the system. The Fock term V_F can be regarded as unique local potentials which correct for the self-interacting problem encountered in V_H. This is due to the "-" sign in V_F which takes into account for the antisymmetric nature of a fermionic system.

2.2 Pairing Correlations

Nucleons of opposite spin and momenta can be paired up to achieve lower energy states compared to their unpaired counterparts, leading to a net lowering of the total energy of the system. This effect is particularly evident in nuclei with even number of nucleons. These interactions are described by the pairing correlations, defined as short-ranged, attractive, nucleon-nucleon forces.

Within the Bogoliubov formalism, the sum over all possible pairs of nucleons leads to the emergence of a collective superfluid state. This state is characterized by the coherent motion of nucleon pairs and can be effectively described using quasi-particles [7].

2.3 Hartree-Fock-Bogoliubov (HFB) and Hartree-Fock + BCS (HF+BCS)

The Hartree-Fock-Bogoliubov (HFB) theory and the BCS (Bardeen-Cooper-Schrieffer) theory both address pairing correlations within quantum many-body systems, but they do so through different approaches. In the HFB theory, the Bogoliubov transformation is applied to the Hartree-Fock Hamiltonian, incorporating pairing correlations within the system. Conversely, in the HF+BCS approach, the pairing correlations are treated subsequent to the HF calculation.

In the BCS model, the concept of quasi-particles treats the system's ground state as a "vacuum" with respect to these quasi-particles. Bogoliubov's work introduced a linear correlation between these quasi-particles and the "bare" particles of the system, effectively incorporating the pairing correlations within the HFB approximation [7].

2.3.1 Hartree-Fock-Bogoliubov (HFB) Theory

The Hartree-Fock-Bogoliubov (HFB) theory involves applying the so-called Bogoliubov transformation to the Hartree-Fock (HF) Hamiltonian to incorporate pairing correlations within the system. This introduces a new field, known as the pairing field [7].

Within the HFB framework, the ground state of the many-body system, denoted as $|0\rangle$, is obtained as a vacuum or reference state with respect to the quasi-particles. The wave function which fulfills this condition is called the HFB wave function, denoted as $|\Phi\rangle$. The bare vacuum state represented by $|-\rangle$ signifies the absence of particles. The ansatz for the HFB ground state is then given by [7]:

$$|\Phi\rangle = \prod_{k=1} \beta_k |-\rangle, \quad \text{where} \quad \beta_k|\Phi\rangle = 0 \quad \text{for all} \quad k = 1, \ldots, M.$$

Here, β_k represents the quasi-particle annihilation operator introduced in Appendix B.

Similar to the derivation of the HF equation, the general Hamiltonian applied here consist of a one-body and two-body density dependent term [9]:

$$H = \sum_{l_1 l_2} t_{l_1 l_2} c^\dagger_{l_1} c_{l_2} + \frac{1}{4} \sum_{l_1 l_2 l_3 l_4} \overline{v}_{l_1 l_2 l_3 l_4} c^\dagger_{l_1} c^\dagger_{l_2} c_{l_4} a_{l_3},$$

where $\overline{v}_{l_1 l_2 l_3 l_4} = \langle l_1 l_2 | v | l_3 l_4 \rangle - \langle l_1 l_2 | v | l_4 l_3 \rangle$.

Analogous to the HF solution, the approximation of the exact ground state is obtained using the variational approach [9]:

$$\delta E[\rho, \kappa] = \delta \frac{\langle \Phi | H | \Phi \rangle}{\langle \Phi | \Phi \rangle} = \delta \left[\mathrm{Tr} \left((t + \frac{1}{2}\Gamma)\rho - \frac{1}{2}\Delta\kappa^* \right) \right] = 0.$$

With the self-consistent fields Γ and Δ defined as:

$$\Gamma_{ij} = \sum_{kl} \overline{v}_{iljk}\rho_{kl} \ , \qquad \rho_{kl} = \langle\Phi|c_l^\dagger c_k|\Phi\rangle = \left(V^* V^T\right)_{ij} ,$$
$$\Delta_{kl} = \frac{1}{2}\sum_{ij} \overline{v}_{ijkl}\kappa_{kl} \ , \qquad \kappa_{ij} = \langle\Phi|c_l c_k|\Phi\rangle = -\left(UV^\dagger\right)_{ij} .$$

Here, ρ and κ denote the density matrix and the pairing tensor respectively. Γ represents the self-consistent Hartree Fock (HF) field, while Δ is the self-consistent pairing field.

Variation of $E[\rho, \kappa]$ with respect to both ρ and κ results in the final HFB equation:

$$\begin{pmatrix} \hat{h} - \lambda & \hat{\Delta} \\ -\hat{\Delta}^* & -(\hat{h}^* - \lambda) \end{pmatrix} \begin{pmatrix} U_k \\ V_k \end{pmatrix} = E_k \begin{pmatrix} U_k \\ V_k \end{pmatrix} .$$

2.4 Skyrme Interaction

$$V = \sum_{i<j} \underbrace{V(i,j)}_{\text{two-body term}} + \sum_{i<j<k} \underbrace{V(i,j,k)}_{\text{three-body term}} \tag{9}$$

The Skyrme interaction [10] provides a framework to describe the effective interaction potential between nucleons within the nucleus. It is expanded from a general many-body interaction represented by Eq. 9, comprising of both a two-body and a three-body term. The two-body term is expanded in terms of low momentum in k-space, reflecting the physical constraint that the nucleons are bounded within the nucleus and thus exhibit limited momentum. The three-body term assumes a zero-range δ force, significantly simplifying the expression.

The result of this expression yields several free parameters that are fitted to various phenomenological data. Examples include the SkM* [11], SLY4 [12], and UNEDF0,1 [13, 14] parametrizations. Each parametrization corresponds to a specific set of coupling constants that are fitted to experimental data such as nuclear binding energies, charge radii, and excitation spectra. These parametrizations provide different levels of accuracy and are tailored to different nuclear systems and phenomena.

The SLY4 parametrization focuses primarily on spectroscopic properties and equation of state of neutron-rich matter such as neutron stars. On the other hand, UNEDF puts emphasis on heavier and deformed nuclei for fitting, with the aim to achieve a more accurate description of nuclear properties.

2.5 Multipole Moments and Beta Parameters

The multipole moment, Q_l is an intrinsic quantity derived from an expansion in spherical harmonics. It describes how the shape is deformed relative to a perfect sphere. In experimental settings, this amounts to the electric multipole moments, which correspond to deviations in the charge distribution from spherical symmetry and can be measured using

spectroscopic techniques. These measurements offer valuable insights into the complex shapes of the nucleus.

With the assumption of axial symmetry, we define the quadrupole and octupole moment operators, denoted as $\hat{Q}_2$ and $\hat{Q}_3$ respectively, in Cartesian coordinates as:

$$\hat{Q}_2 = \langle 2Z^2 - X^2 - Y^2 \rangle,$$
$$\hat{Q}_3 = \langle Z(2Z^2 - 3X^2 - 3Y^2) \rangle.$$

Here, Z represents the symmetry axis, while X and Y correspond to the perpendicular axes.

The multipole moments can then be quantified by a unit-less deformation parameter β_l to describe the deformation of a nucleus while also accounting for volume conservation [15]. The deformation parameter β_l is defined here to be:

$$\beta_l = \frac{\sqrt{(2l+1)\pi}}{3} \frac{Q_l}{A[R_0]^l},$$

where A is the mass number of the nucleus, Q_l is the intrinsic multipole moment of order l, and the nuclear radius defined as $R_0 = 1.2[\text{fm}]$. A detailed derivation of both Q_l and β_l is provided in Appendix C.

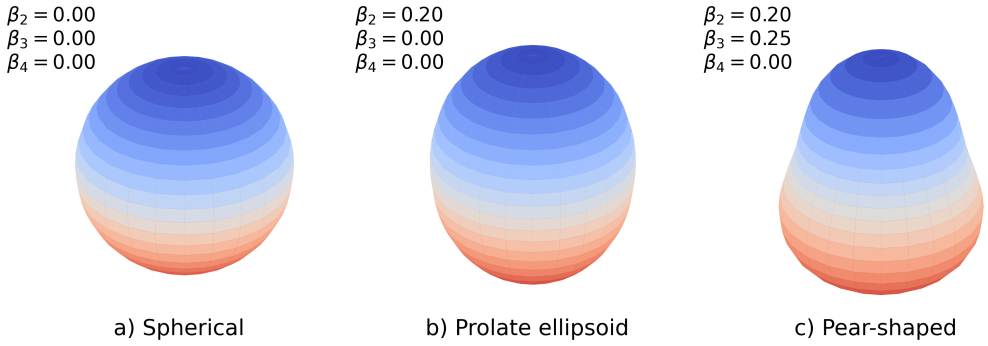

Fig. 1: Visualization of common nuclear shapes represented by deformation parameters β_l using Eq. 10.

A radial function function depending on the polar angle [15],

$$R(\theta) = R_0 \left[1 + \sum_{l=2}^{l_{\max}} \left(\beta_l Y_{l0}(\theta) - \frac{[\beta_l]^2}{4\pi} \right) \right] \tag{10}$$

can be expressed in terms of spherical harmonics, $Y_{l0}(\theta)$ and the deformation parameters, β_l to efficiently characterise the axially deformed shapes of nuclei. This is shown in Fig. 1, which it illustrates various common nuclear shapes plotted using $R(\theta)$.

2.6 Nilsson Model and the Particle + Rotor Model

The Nilsson model [16] is based on the combination of the deformed single-particle model and the rotor scheme [17], which assumes that the valence nucleon moves in a deformed potential created by a rotating even-even core. This integration enables the generalization of the shell model to deformed nuclei, especially for odd-mass deformed nuclei. With the assumption of axial symmetry, the total spin is given to be $I = j + R$. j represents the single-particle angular momentum and R is the collective rotation of the system, which is perpendicular to the symmetry axis (z-axis). This is illustrated in Fig. 2a).

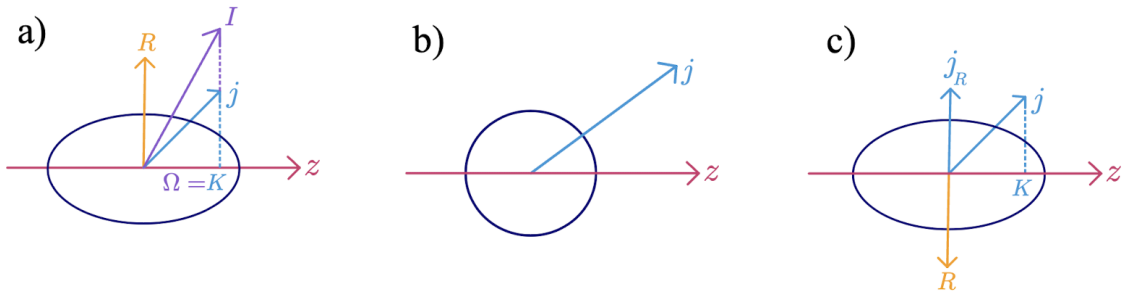

Fig. 2: Visualization of the single-particle + rotor model with different coupling schemes. a) General depiction of the model. b) Weak coupling scheme. c) Strong coupling scheme.

For small deformation ($|\beta_2| \lesssim 0.1$), we assume $R = 0$, as the moment of inertia $\mathcal{J}$ will be small for a spherical nucleus. This is the case for nuclei with / close to closed shells. The even-even core of the nucleus will have a larger energy spacing compared to the energy spacing between the single-particle states. Hence, we get that $I \approx j$. This is commonly known as the "weak coupling" scheme, as depicted in Fig. 2b).

In the case of a well deformed nucleus, the "strong coupling approximation" is implemented, as shown in Fig. 2c). It postulates that the projection of both I and j onto the symmetrical axis, K and Ω respectively, would be equivalent $K = \Omega$.[2] This assumption arises from considering R to be orthogonal to the symmetry axis and therefore does not contribute to the projections. This configuration is found to have the lowest energy and is expected to be favored in ground states [17]. It may also be appropriate to assume that in the ground state, the core may rotate such that R cancels out j_R, the projection of j onto R, resulting in the lowest possible I. This leads to the approximation of $I \approx K$ in this regime.

In the Nilsson model, each value of j corresponds to $(2j+1)$ orbitals, which are represented by sets of Nilsson quantum numbers. These sets of quantum numbers are denoted by $\Omega^{\pi}[Nn_z\Lambda]$ in the cylindrical basis. N represents the principal quantum number and π is the parity of states $(-1)^N$. Assuming that the axis of the symmetry is the z-axis, Ω is the projection of the s.p angular momentum j along the z-axis, n_z is the number of quanta along the z-axis of the anisotropic harmonic oscillator potential and Λ is the projection of the orbital angular momentum onto the z-axis. The quantum numbers projected onto

[2] K and Ω may be used interchangeably in this scheme.

the symmetry axis are considered approximately good quantum numbers. This means that they remain unchanged throughout the system's motion due to the assumed axial symmetry.

Furthermore, K is equivalent to the band head's angular momentum in a rotational band. Consequently, the lowest band head corresponds to the ground state of an odd-mass nucleus. This concept is vital for comparing our predictions to experimental data.

3 Computational Programs

The computational programs implemented in this study consist of the HFBTHO codes, namely HFBTHOv2 [18] and HFBTHOv4 [19] and the SkyAx code [20]. These codes were chosen mainly due to their easy accessibility online and well-established benchmarks. We assume default values for the parameters, unless specifically specified.

3.1 HFBTHO Code

HFBTHO [19, 18] is a computational code proficient at solving Skyrme-Hartree-Fock-Bogoliubov (HFB) equations. It employs axial symmetry to reduce computational complexity and utilizes a Harmonic oscillator basis for expanding quasi-particle wave functions. The program achieves the self-consistent solution by iteratively diagonalizing the HFB Hamiltonian using Skyrme-like energy densities and zero-range pairing interactions. This approach accurately represents the system's nuclear structure, especially in deformed nuclei, while optimizing computational efficiency.

3.2 SkyAx Code

SkyAx [20] is a computational program designed to solve the Hartree–Fock (HF) equations using a two-dimensional mesh, incorporating Skyrme functionals and axial symmetry. Moreover, SkyAx includes pairing interactions separately using BCS theory. Unlike the iterative diagonalization method used in the HFBTHO code, SkyAx employs a damped gradient iteration method to approach the solution. This method not only requires less computational resources but also enables SkyAx to be faster compared to HFBTHO.

4 Findings

The range of Radium isotopes, from Ra212 to Ra228, serves as a starting point for this analysis. Previous studies [21, 22] have highlighted this region for its notable octupole deformation. Moreover, it includes isotopes known to exhibit extremely small parity doublet separations [3].

4.1 Even Radium (Ra) Isotopes

To obtain a simplified overview of the Ra isotopes, we initially focused solely on constraining Q_2. Additionally, we employed the Nilsson diagram to enhance our comprehension of the correlation between the shapes and the energy of the nucleus.

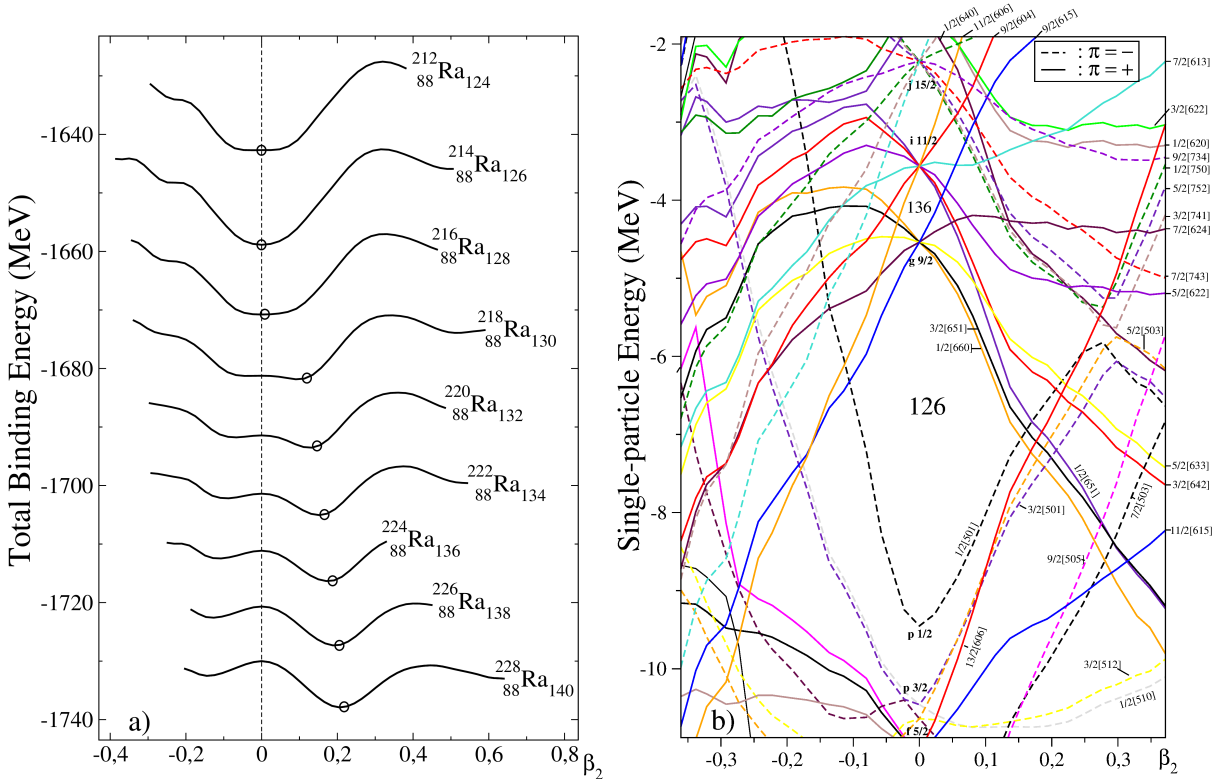

Fig. 3: a) Plot showing quadrupole Q_2 constraints of even Ra isotopes with octupole $Q_3 = 0$ obtained using HFBTHOv4, UNEDF1 and 16 oscillator shells. b) Diagram depicting Nilsson orbitals plotted against β_2 for neutrons, computed using HFBTHOv2, SLY4, and 16 oscillator shells for Ra216.[3]

The isotopes presented in Fig. 3a) are denoted as ${}^{A}_{Z}\mathrm{X}_{N}$, where A represents the total number of nucleons, Z indicates the proton number and X is the element.

In Fig. 3a), a few distinct trends are apparent. Firstly, as the mass of the even Ra isotopes increases, a consistent decrease of the energy minimas are observed. This is expected of

[3]It is important to note that β_2 in Fig. 3 were computed from HFBTHOv2, and that β_2 mentioned here refers to these computed values.

medium to heavy nuclei, as the nuclear binding energy per nucleon is fairly constant in this regime $\approx$ 8MeV [7]. This explains the increased binding of nucleus and the relatively uniform energy decrease when additional pairs of neutrons are added. Subsequently, there is a clear shift to the right ($\beta_2 > 0$) in the energy minima as mass increases, implying a deformation towards more prolate shapes. As the isotopes deviate from the magic number ($N = 126$), they become more deformed as it is much more energetically favourable. This trend can be understood from Fig. 3b), where above $N = 126$, the single-particle states become more bounded as β_2 increases positively. Another interesting observation is that Fig. 3a) suggests that Ra212 to Ra216 would likely have a spherical or relatively spherical shape ($\beta_2 \approx 0$). The trend observed also suggests that the increase in β_2 becomes less pronounced as we move from Ra218 to Ra228, indicating a slower rate of change in nuclear deformation compared to lighter isotopes. However, it's important to note that these findings offer only a partial understanding of isotope stability, as they solely focus on the quadrupole moments.

For consistency, the labeling of the Nilsson orbitals in Fig. 3b) were obtained from the solutions at which the quadrupole constraints were set to $Q_2 = 17$, $\beta_2 \approx 0.19$. It was observed that the Nilsson labels, computed by the HFBTHOv2 code, may vary depending on the regions $|\beta_2| \lesssim 0.1$, $|\beta_2| \lesssim 0.2$, and $|\beta_2| \gtrsim 0.25$.

N, Orbital	**Skyrme-HFB Potential**	**Deformed Harmonic Osc.**
5, p1/2	1[501]	1[501]
6, g9/2	1[660]	1[651]
	3[651]	3[642]
	5[633]	5[633]
	7[624]	7[613]
	9[615]	9[604]
6, i11/2	1[651]	1[640]
	3[642]	3[631]
	5[622]	5[622]
	7[613]	7[624]
	9[604]	9[615]
	11[606]	11[606]
6, d5/2	1[640]	1[631]
7, j15/2	1[750]	1[770]
	3[741]	3[761]
	5[752]	5[752]
	7[743]	7[743]
	9[734]	9[734]

Table 1: Comparison of relevant Nilsson labels obtained from the Skyrme-HFB potential using HFBTHOv2 at $\beta_2 \approx 0.19$, and those derived from assuming a deformed harmonic oscillator (Osc.) [23].

The experimental interpretations of this region $|\beta_2| \lesssim 0.25$ are often labeled using the Nilsson assymptotic quantum numbers $\Omega^\pi[Nn_z\Lambda]$. However, these quantum numbers ob-

tained from self-consistent solutions with Skyrme interactions may deviate from the ones obtained using a pure oscillator model. This is especially true for smaller deformations $|\beta_2| \lesssim 0.1$. Therefore, Table 1 serves as a comparison of these Nilsson labels from both approaches.

4.1.1 Shapes of Even Ra isotopes

To proceed with our investigation, a full HFB+BCS treatment was applied to these isotopes by utilising the SkyAx code.

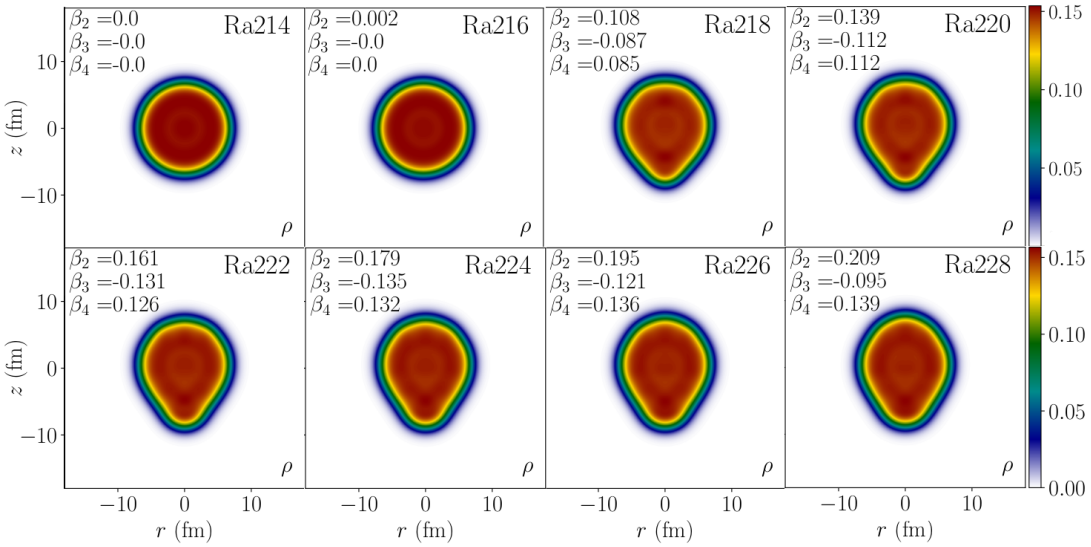

Fig. 4: Cross-sectional density plot generated using SkyAx, UNEDF1. The colour map here illustrates the density of the nucleus, ρ [nucleons/(fm^3)]. The axis of symmetry and the radial axes are represented by z and r respectively. Unlike β_2, the negative sign for β_3 is not of any importance as it merely dictates the orientation of the symmetry axis.

The results are shown in Fig. 4. In this figure, Ra214 and Ra216 appear to exhibit little to no deformation. As the mass increases from Ra218 to Ra228, the rate of increase of β_2 drops. The trends observed here appear to align well with our interpretation of Fig. 3. With a full minimization, Ra218 to Ra228 were predicted to have an octupole deformation. This octupole deformation, characterized by β_3, is observed to increase from Ra218 to Ra224, after which it starts to decrease.

The alignment of these trends indicate that the isotope with the largest β_3 falls within the range of Ra220 to Ra226, consistent with findings from previous studies [22, 24].

4.2 Analysis of Different Skyrme Models

The calculations for the octupole deformation of even Ra isotopes were performed on the HFBTHOv2, HFBTHOv4, and the SkyAx codes. The HFBTHO codes were ran first with constraints and without Lipkin-Nogami (LN) to probe the nuclei to be deformed, then it is restarted with LN and applying "kick-off" mode, where the first 10 iterations are

constrained and released thereafter. The Lipkin-Nogami (LN) method [25, 26] is applied to approximately restore the particle numbers before variation.

When parity is broken, in the case of octupole deformed nuclei calculations, the centre of mass of the nucleus may drift along the symmetric axis. This effect is mitigated in the HFBTHO codes by constraining the dipole moment, Q_1 to 0 throughout all calculations. For the SkyAx code, this issue is inherently taken into account by a shift operator acting on each single-particle wave function while also constraining Q_1 to 0.

A recent study, on the basis of SLY4 and SKM* concluded that the octupole deformation of Ra isotopes is highly dependent on the Skyrme parameterization [24]. Taking this into consideration, the pairing interaction parameters for both neutrons and protons, denoted by "vpair_n" and "vpair_p" were set to -258.2. This adjustment was then applied to all proceeding HFBTHO calculations using the SLY4 parameterization. The pairig potentials for the other parameterizations in both the HFBTHO and SkyAx codes were set as default values.

The experimental data denoted as Exp. in Fig. 5 are derived from Q_l values obtained through experimentally fitted rotational models based on measurements of electric transitions [21]. Since these measurements only involve contributions from protons, we infer that each nucleon equally contributes to the intrinsic multipole moment, which is then converted to β_l using Eq. 12. Additionally, alongside the experimental data, we use the results from another nodel, namely the Finite-Range Droplet Model (FRDM) [27] as a benchmark for our calculations. The FRDM employs a macroscopic-microscopic approach, which is based on the droplet model with finite-range nuclear forces to describe nuclear properties.

In Fig. 5a) and b), both β_2 and β_3 were derived from the Q_2 and Q_3 values obtained from the HFBTHO codes. It is gathered that these multipole moments Q_l may have been defined differently in the HFBTHO codes, with Q_2 defined by Eq. 11 and Q_3 by Eq. 13. Consequently, β_2 was calculated using Eq. 12, while β_3 was derived from Eq. 13. Additionally, both β_2 and β_3 values were directly obtained from the SkyAx results. According to the SkyAx documentations [20], the final definitions of β_l should match those calculated from the HFBTHO codes.

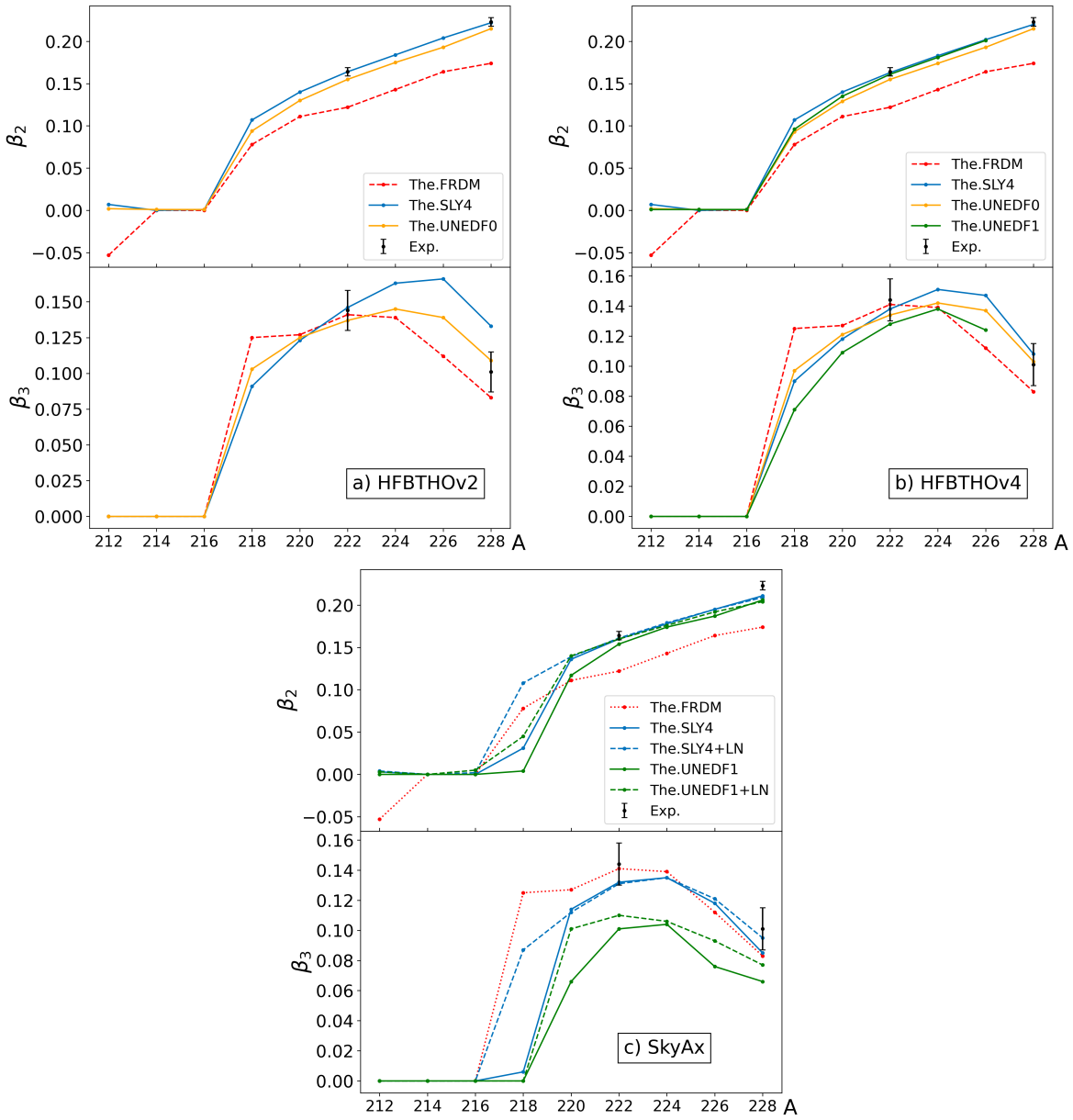

Fig. 5: comparison of calculations using different Skyrme functionals and codes with experimental data and results from the FRDM, showcasing β_2 and β_3 values plotted against Ra isotopes. The experimental data is denoted as (Exp.).

Comparing the results presented in Fig. 5, it is evident that, with the exception of FRDM, HFBTHOv2:SLY4, and SkyAx:UNEDF1+LN, the examined models consistently predict Ra224 to have the highest β_3 value. However, FRDM and SkyAx:UNEDF1+LN differ, suggesting Ra222, while HFBTHOv2:SLY4 predicted the peak to be at Ra226, in agreement with previous calculations which also incorporated a lower pairing potential for SLY4 [24]. Experimental findings suggest an increase in β_3 from Ra224 to Ra226 [28], which is only predicted by HFBTHOv2:SLY4. These predictions regarding the region of largest β_3 are also consistent with results from previous studies [22, 24]. It is worth mentioning that despite numerous attempts, the self-consistent solution of the HFBTHOv4:UNEDF1

model for Ra228 failed to converge.

In Fig. 5c), the SkyAx models illustrate the influence of incorporating LN (Lipkin-Nogami) corrections in the calculations. It is observed that both models, when including LN, predict values closer to the experimental data compared to their counterparts without LN corrections. Additionally, It was noted in the SkyAx documentation [20], that the pairing interaction is defined differently for different Skyrme parameterizations for the code. The pairing potential for SkyAx is density dependent while UNEDF1 assumes a delta-function.

The tabulated results from both the HFBTHO codes are gathered in both Table 3 and 4 for reference.

4.3 Odd Radium (Ra) Isotopes

4.3.1 Initial Survey of Odd Ra Isotopes Using Quasi-particles

A preliminary analysis of the odd Ra isotopes was conducted using the quasi-particle approach in the HFBTHO code. This method treats quasi-particles as "blocking candidates", allowing for the addition or removal of a quasi-neutron from an even nucleus. The term "blocking candidates" refer to specific quasi-particle states energetically favoured by the valence neutron. The HFBTHO codes are capable of listing out these states within 2MeV of the neighbouring even nucleus it computes on, provided that it is activated. However, comprehensive self-consistent calculations for odd systems have not been extensively explored due to the considerable time investment required.

The "blocking candidates" described below were directly obtained from calculations on even Ra isotopes using the HFBTHOv2 code. In this analysis, we assumed that a nucleon is removed from a filled orbital.

Isotopes	**Ground state Ψ_0**		**First excited band head Ψ_1**	
	I^π	**Interpretation**	I^π	**Interpretation**
Ra215	$9/2^+$	ν (g$9/2^+$)	-	-
Ra217	$9/2^+$	ν (g$9/2^+$)	$11/2^+$	ν i$11/2^+$
Ra219	$I = 7/2^+, K = 1/2,$ ν (1+[651])*, i$11/2^+$		; $I = 9/2^+, K = 5/2,$ ν (5+[633])*, g$9/2^+$	
Ra221	$5/2^+$	ν (5+[633]), g$9/2^+$	$5/2^-$	ν (5-[752])*, j$15/2^{-}$*
Ra223	$3/2^+$	ν (3+[631]), i$11/2^+$	$3/2^-$	ν (3-[761]), j$15/2^-$
Ra225	$1/2^+$	ν (1+[640])*, d$5/2^+$*	$3/2^-$	ν (3-[741])*, j$15/2^{-}$*
Ra227	$3/2^+$	ν (3+[631]), i$11/2^+$	$5/2^+$	ν (5+[633]), g$9/2^+$

Table 2: Experimental data for j and K quantum numbers obtained from [29] and findings for Ra219 from [29, 30]. In this table, ν represents the valence neutron placed in the specified Nilsson orbital configuration $2\Omega^\pi[N\ n_z\ \Lambda]$. The asterisk (*) indicates the interpretation and labels based on experimental I, Fig. 3b) and Table 1.

From the tabulated data in Table 2, the lowest-lying band head of the rotational bands from experimental data [29] is treated as the ground state, Ψ_0, while the subsequent lowest-lying band head is represented as Ψ_1. In Section 2.6, it was inferred that the total spin of the system, denoted as I, is interpreted here as j for Ra215 and Ra217, which exhibit little to no deformation. However, for Ra221 to Ra227, where stronger deformations are observed, I is treated to be K instead.

Since Ra219 lies within the transitional region, it is treated differently. The Ra219 data, highlighted in blue in Table 2, presents the interpretation of experimentally observed I from a recent study [30].

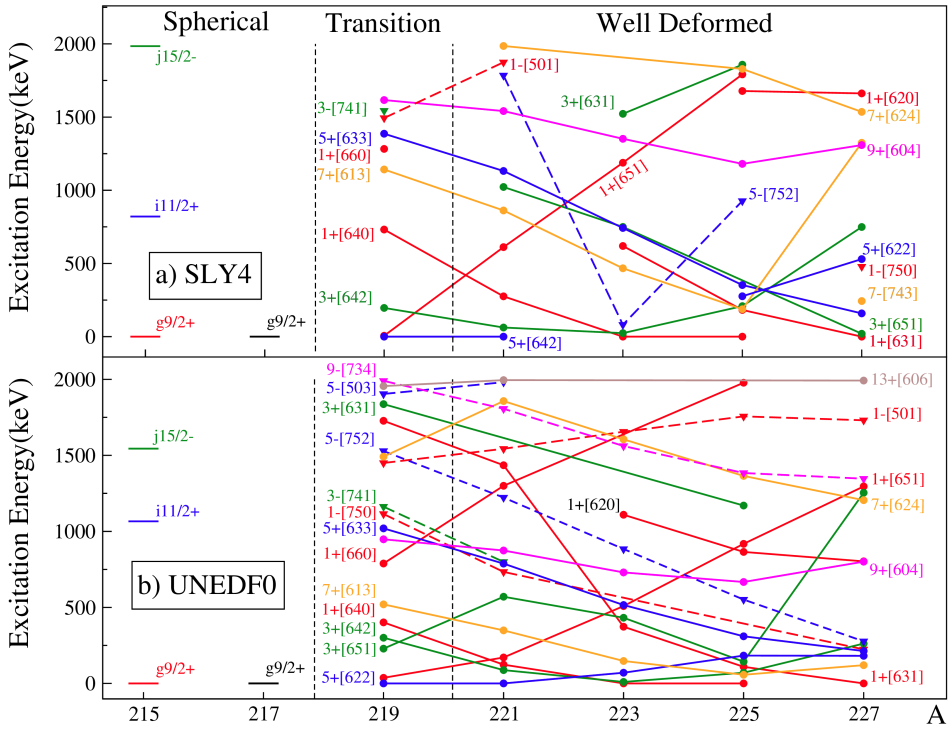

Fig. 6: Quasi-neutron energy calculations for Ra215 to Ra227, obtained from neighboring even nuclei using HFBTHOv2 with different Skyrme functionals: (a) SLY4 and (b) UNEDF0. The Nilsson labels are represented as $2\Omega^{\pi}[N\ n_z\ \Lambda]$ and are obtained from the code. The excitation energy here is taken to be the difference between the quasi-neutron energy and the predicted ground state energy. [4]

Fig. 6 designates three regions based on the predicted shape of the nuclei: Spherical, Transition, and Well Deformed. In the Spherical region, only the j-shells were considered for these nuclei with small deformations ($|\beta_2| \lesssim 0.1$). For well-deformed nuclei, Nilsson labels were employed to characterize the valence neutron. Within the spherical region, both models predicted g9/2+ as the ground state, agreeing with experimental observations. The subsequent arrangement of j-shells of both predictions are the same albeit the energy gaps between subsequent j-shells differ. With SLY4 having a larger gap between

[4] Ra217 has been left out and discussed separately in Fig. 7.

g9/2+ and i11/2+, while UNEDF0 has a larger energy gap between i11/2+ and j15/2−.

In the transition region, a ground state $K = 5/2$ of Ra219 was predicted by both models, although the Nilsson labels differ. The predicted $K = 5/2$ state agrees with the interpretation for the experimentally observed first excited band head with $I = 9/2+$, based on theoretical calculations from recent study [30]. This is inferred to be the odd neutron occupying the g9/2+ orbital with $K = 5/2$. In Fig. 3, this is labeled as 5+[633], according to Table 1. The experimentally observed $I = 7/2+$ is deduced to stem from the valence neutron occupying the i11/2+ orbital with $K = 1/2$. This orbital labeled as 1+[651] in Fig. 3 is predicted to be close to the ground state for both models, matching experimental observations [29]. The energy for the predicted 1+[651] state is approximately 6.4keV and 31.4keV respectively for SLY4 and UNEDF0.

In the well-deformed region, both models predicted Ra221 to have a ground state based on $K = 5/2$, in agreement with experimental observations, despite originating from different orbitals, as shown in Fig. 6. The experimental band head state interpreted as originating from 5+[633] was also anticipated by both interactions albeit at higher energies (SLY4=1131.69keV, UNEDF0=788.489keV). The subsequent experimentally observed band head with $I = 5/2−$, inferred to stem from 5-[752], was also found by both models (SLY4=1784.6keV, UNEDF0=1222.52keV).

For Ra223, both models predicted a state with $K = 3/2$, closely situated to the predicted ground state at 24.1258keV and 10.0607keV for SLY4 and UNEDF0 respectively. This aligns with the 3+[631] state, deduced from experiment. This orbital is labeled as 3+[642] in Fig. 6 as referenced from Table 1. The next lowest band head observed in the experiment originates from occupying the 3-[761] orbital. This orbital, identified as 3-[741] in Fig. 6, was not predicted by either models.

Based on the experimentally observed $I = 1/2+$, the ground state for Ra225 was inferred to derive from occupancy of the 1+[640] orbital. This is in agreement with the predictions of both models. However, the subsequent observed band head, deduced to be attributed to the 3-[741] orbital from Table 1 and Fig. 3, was not found by both models.

The calculated ground state of Ra227 from both interactions was obtained to be 1+[631], as shown in Fig. 6. Meanwhile, the lowest-lying band head observed experimentally is interpreted to arise from 3+[631], depicted as 3+[642] in Fig. 6, according to Table 1. This configuration is predicted by both models, with 3+[642] being much closer to the ground state for UNEDF0 (at 262.543keV), while SLY4 at 749.057keV. The following band head from experiment, deduced to originate from 5+[633] was also successfully found by both interactions, however, at lower energies compared to the 3+[642] state (SLY4=362.056keV and UNED0=213.368keV).

Experimental observations have indicated the presence of parity doublets $I = 3/2±$ and $I = 1/2±$ in Ra223 and Ra225, respectively [3, 6]. However, these parity doublets are not predicted by our calculations, as parity is not restored in this analysis. Only upon restoration would each mean-field state provide two experimentally observed states (parity

doublets). A simplified comparison, focusing only on the ground states and the first two excited states of the Ra isotopes in the well deformed region is presented in Appendix D Fig. 9.

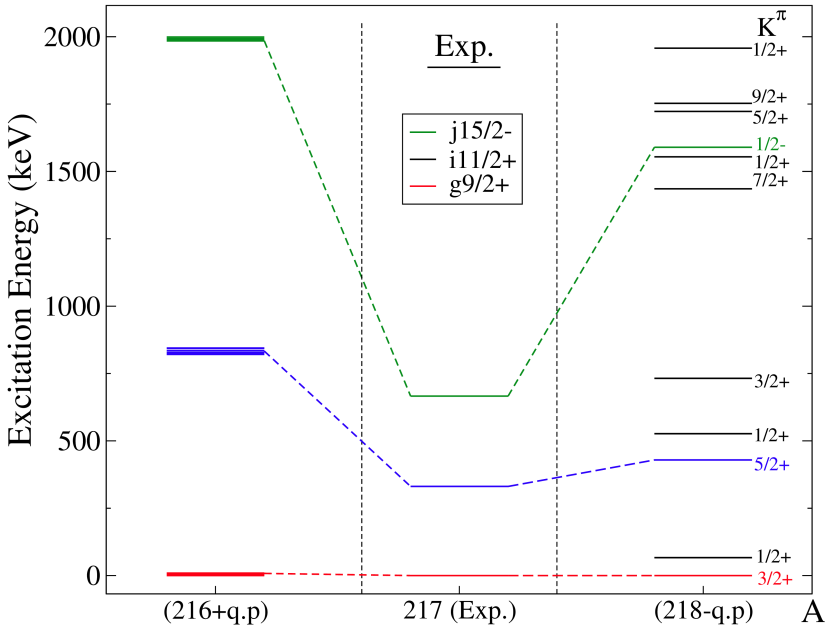

Fig. 7: Comparison between quasi-neutron energies predicted by both neighbouring even isotopes of Ra217 and experimental data of Ra217 [29], denoted as (Exp.). The predictions are obtained from the solutions of HFBTHOv2 employing SLY4.

The Exp. energy levels depicted in Fig. 7 were interpreted in similar fashion as in Table 2. The ground state is inferred as the lowest-lying band head observed in the experiment, and the subsequent states are identified as the next lowest band heads.

Fig. 7 presents the quasi-neutron energy calculations for the even Ra isotopes, Ra216 and Ra218, denoted as (216+q.p) and (218-q.p) respectively, alongside experimental data for Ra217. Starting from the deformed Ra218 (218-q.p), we plotted all the quasi-neutron energies, with coloured labels indicating the interpreted lowest K originating from each j-shell: g$9/2^+$, i$11/2^+$, and $j15/2^-$ based on Fig. 3 and Table 1.

It is observed in Fig. 7 that (216+q.p) displays large energy gaps with degenerate orbital energy levels, resembling Fig. 3b) at $\beta_2 = 0$. At (218-q.p), energy gaps between these interpreted orbitals appear to lie closer to experimental values and the energy levels appear more spread out, resembling those in the well-deformed region presented in Fig. 6.

These observations suggest that Ra217 may occupy a transitional region. It was also highly predicted in Fig. 5 that the Radium isotopes start to deform after Ra216, further corroborating this notion.

5 Conclusion

Nuclei undergoing spontaneous symmetry breaking adopt a pear shape. Upon symmetry restoration, this leads to the formation of closely spaced parity doublets, resulting in a heightened sensitivity to $\mathcal{CP}$-violating effects. In this work, the utilization of low-momentum Skyrme-type interactions has proven effective in predicting the shapes of Radium nuclei, reproducing observed trends in nuclear structure. In addition, the predictions of spins for both the ground state and excited state have been shown to be in good agreement with experimental observations. This study has also demonstrated that the octupole deformation is highly sensitive to the strength of pairing potential, with the HFBTHOv2:SLY4 model using modified pairing potential exhibiting the highest performance.

Based on these findings, we advocate for further exploration through full many-body calculations, employing these inter-nuclear potentials and incorporating symmetry restoration techniques. Emphasizing the optimization of pairing potential strengths and conducting systematic assessments of nuclear Schiff moments is expected to yield significant advances in our understanding of $\mathcal{CP}$-violation.

Acknowledgements

I would like to take this opportunity to extend my gratitude to my supervisor, Gillis. Throughout the past months, his guidance and patience have been invaluable, as he devoted his time to personally explain complex topics relevant to our study. He has also helped with figuring out the problems encountered during this project, such as with the definition of β_l. Additionally, I am thankful to him for allowing me to visit his office whenever I had questions or needed guidance

Appendix A: Slater Determinant

A Slater determinant is described as an anti-symmetrized product of single-particle wave functions to describe a multi-fermionic system with A particles [9]:

$$\Phi_A(\mathbf{r}_1, \mathbf{r}_2, \ldots, \mathbf{r}_A) = \mathcal{A}\left[\phi_1(\mathbf{r}_1)\phi_2(\mathbf{r}_2)\ldots\phi_A(\mathbf{r}_A)\right],$$

The operator $\mathcal{A}$ in the expression ensures that all possible permutations of the single-particle wave functions are considered, while also normalizing the Slater determinant to fulfill the anti-symmetric condition:

$$\Phi_A(\mathbf{r}_1, \mathbf{r}_2, \ldots, \mathbf{r}_A) = \frac{1}{\sqrt{A!}}\begin{vmatrix} \phi_1(\mathbf{r}_1) & \phi_2(\mathbf{r}_1) & \cdots & \phi_A(\mathbf{r}_1) \\ \phi_1(\mathbf{r}_2) & \phi_2(\mathbf{r}_2) & \cdots & \phi_A(\mathbf{r}_2) \\ \vdots & \vdots & \ddots & \vdots \\ \phi_1(\mathbf{r}_A) & \phi_2(\mathbf{r}_A) & \cdots & \phi_A(\mathbf{r}_A) \end{vmatrix}$$

Appendix B: Bogoliubov Operators

The quasi-particle operators are obtained through a linear transformation from the bare particle operators[5] c_l and $c_l^\dagger$ given by [7]:

$$\beta_k^\dagger = \sum_l U_{lk}c_l^\dagger + V_{lk}c_l.$$

Here, U and V represent coefficients required to fulfill fermionic commutation rules. Both indices k and l span the configuration space from 1 to M. The configuration space here has dimension M which depends on the number of oscillator shells, N_0 used in calculations. This transformation results in operators acting on a $2M$-dimensional space:

$$\begin{pmatrix} \beta \\ \beta^\dagger \end{pmatrix} = \begin{pmatrix} U^\dagger & V^\dagger \\ V^T & U^T \end{pmatrix}\begin{pmatrix} c \\ c^\dagger \end{pmatrix} = \mathcal{W}^\dagger\begin{pmatrix} c \\ c^\dagger \end{pmatrix},$$

where $\mathcal{W}$ is defined as:

$$\mathcal{W} = \begin{pmatrix} U & V^* \\ V & U^* \end{pmatrix}.$$

This linear relationship connects the quasi-particle operators $(\beta, \beta^\dagger)$ with the particle operators $(c, c^\dagger)$.

[5] c_l and $c_l^\dagger$ are known as the particle creation and annihilation operators, β_l and $\beta_l^\dagger$ are known as the quasi-particle creation and annihilation operators.

Appendix C: Derivation of Multipole Moments and Beta Parameters

In general, if an axial symmetry is assumed, the multipole moment operators, Q_l can be written in the form:

$$\hat{Q}_l = \langle r^l Y_{l0}(\theta) \rangle,$$

where r^l represents the radial part of the multipole moment operator and $Y_{l0}(\theta)$ is the spherical harmonic function symmetric around the $Z-$axis.

To simplify the expression, $Y_{l0}(\theta)$ can be rewritten using legendre polynomials as:

$$Y_{l0}(\theta) = \sqrt{\frac{2l+1}{4\pi}} P_l(\cos(\theta)).$$

$P_l(\cos(\theta))$ is the associated Legendre polynomial of degree l.

It is convenient to incorporate an additional factor of $\sqrt{\frac{16\pi}{2l+1}}$ into $\hat{Q}_l$, which simplifies the operators to:

$$\tilde{Q}_l = \langle 2r^l P_l\left(\cos(\theta)\right) \rangle. \tag{11}$$

The additional factor incorporated provides a simpler expression when transformed in cartesian coordinates using $\cos(\theta) = Z/r$ and $r = \sqrt{X^2+Y^2+Z^2}$ leads to:

$$\tilde{Q}_2 = \langle 2Z^2 - X^2 - Y^2 \rangle$$
$$\tilde{Q}_3 = \langle Z(2Z^2 - 3X^2 - 3Y^2) \rangle.$$

The beta parameters β_l is derived from the expansion of the multipole moment Q_l:

$$\begin{aligned}
\tilde{Q}_2 &= \frac{A\int_0^{2\pi}\int_0^{\pi}\int_0^{R(\theta)} \left[r^2 \sin(\theta)\hat{Q}_2\right] dr d\theta d\phi}{\int_0^{2\pi}\int_0^{\pi}\int_0^{R(\theta)} r^2 \sin(\theta)\ dr d\theta d\phi} \\
&= \left(\frac{3A[R_0]^2}{\sqrt{5\pi}}\beta_2 + \frac{6A[R_0]^2}{7\pi}\beta_2^2 + O[\beta_2]^3\right) \\
&+ \left(\frac{4A[R_0]^2}{5\pi} + \frac{117A[R_0]^2}{22\sqrt{5}\pi^{3/2}}\beta_2 + \frac{1431A[R_0]^2}{910\pi^2}\beta_2^2 + O[\beta_2]^3\right)\beta_3^2 + O[\beta_3]^3,
\end{aligned}$$

$$\begin{aligned}
\tilde{Q}_3 &= \frac{A\int_0^{2\pi}\int_0^{\pi}\int_0^{R(\theta)} \left[r^3 \sin(\theta)\hat{Q}_3\right] dr d\theta d\phi}{\int_0^{2\pi}\int_0^{\pi}\int_0^{R(\theta)} r^2 \sin(\theta)\ dr d\theta d\phi} \\
&= \left(\frac{3A[R_0]^3}{\sqrt{7\pi}}\beta_3 + O[\beta_3]^3\right) + \left(\frac{2\sqrt{\frac{5}{7}}A[R_0]^3}{\pi}\beta_3 + O[\beta_3]^3\right)\beta_2 \\
&+ \left(\frac{445A[R_0]^3}{44\sqrt{7}\pi^{3/2}}\beta_3 + O[\beta_3]^3\right)\beta_2^2 + O[\beta_2]^3.
\end{aligned}$$

Here, $R(\theta)$ is the nuclear radius depending on the polar angle θ. This is expressed in terms of β_l,

$$R(\theta) = R_0 \left[1 + \sum_{l=2}^{l_{\max}} \left(\beta_l Y_{l0}(\theta) - \frac{[\beta_l]^2}{4\pi} \right) \right], \text{ where } R_0 = 1.2[\text{fm}] A^{\frac{1}{3}}.$$

Taking only the first-order in the expansion, the general form for β_l (for $l = 2, 3$) is defined as

$$\beta_l = \frac{\sqrt{(2l+1)\pi}}{3} \frac{\tilde{Q}_l}{A[R_0]^l}. \tag{12}$$

Using the definition of $Q_l = r^l \sqrt{\frac{2l+1}{16\pi}} P_l(\cos(\theta))$ would instead yield:

$$\beta_l = \frac{4\pi}{3} \frac{Q_l}{A[R_0]^l}. \tag{13}$$

Appendix D: Supplementary Plots

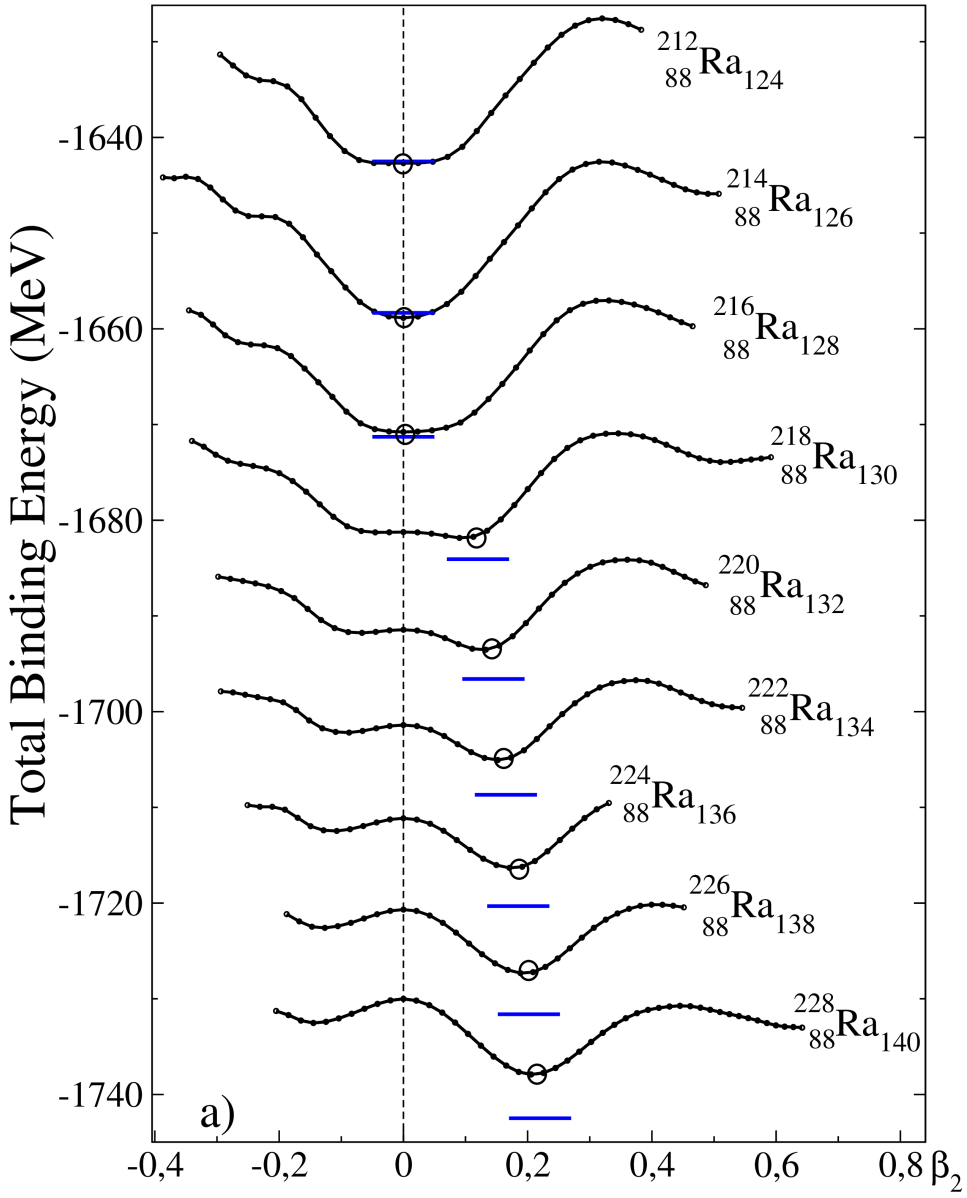

Fig. 8: This plot is the same as Fig. 3a), but with the addition of experimental data[31] for comparison, indicated by the blue lines (—).

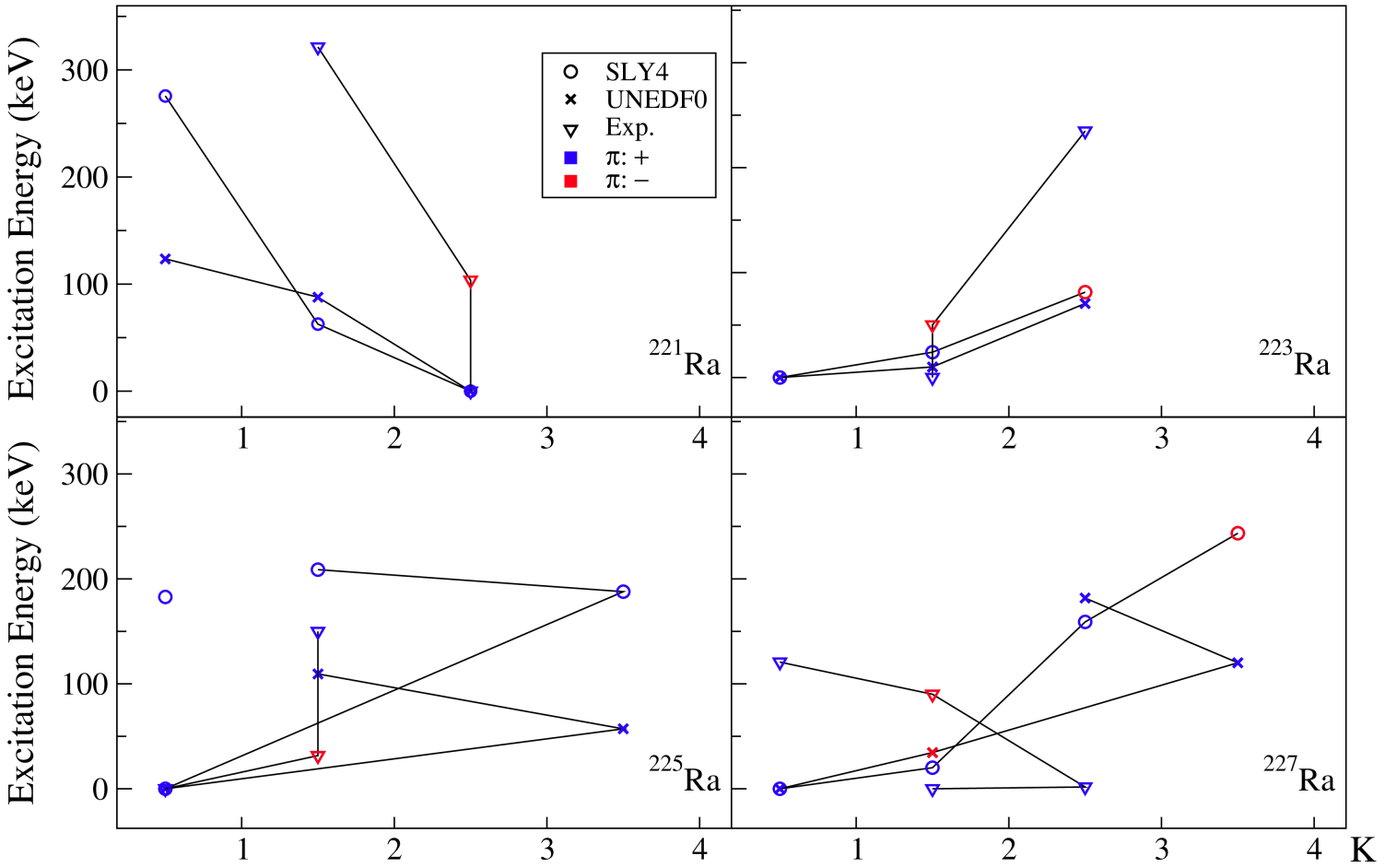

Fig. 9: Comparison of both SLY4 and UNEDF0 predictions obtained from Section 4.3.1 against experimental (Exp.) data[29] for Ra221 to Ra227. The plots depict the evolution of the interpreted spins K from the ground states to the second excited states, represented by the connecting lines. The first and second band heads from Exp. data are inferred to be the first and second excited states, respectively.

Appendix E: Tabulated Results and Data

SLY4, $N_o = 20$						
Ra	Q_2 (fm^2)	Q_3 (fm^3)	β_2^*	β_2	β_3	**B.E (MeV)**
212	59.337	0.003	0.007064	0.007	0.000	-1636.598237
214	3.580	0.001	0.00042	0.000	0.000	-1653.609856
216	5.919	0.002	0.000683	0.001	0.000	-1664.850360
218	922.407	1787.047	0.104112	0.107	0.091	-1676.453180
220	1227.410	2462.391	0.135640	0.140	0.123	-1688.711284
222	1450.699	2970.456	0.157176	0.164	0.146	-1700.050138
224	1656.612	3379.353	0.176059	0.184	0.163	-1710.693816
226	1867.562	3496.320	0.194869	0.204	0.166	-1720.842240
228	2061.648	2850.745	0.211721	0.222	0.133	-1730.431135
UNEDF0, $N_o = 20$						
Ra	Q_2 (fm^2)	Q_3 (fm^3)	β_2^*	β_2	β_3	**B.E (MeV)**
212	16.365	0.011	0.001953	0.002	0.000	-1641.378739
214	4.326	0.008	0.000508	0.001	0.000	-1658.210568
216	7.429	0.004	0.000859	0.001	0.000	-1670.940753
218	805.795	2022.049	0.091047	0.094	0.103	-1683.448688
220	1131.728	2486.98	0.125223	0.130	0.125	-1695.921126
222	1374.331	2787.868	0.149067	0.155	0.137	-1707.841926
224	1571.822	3001.201	0.167296	0.175	0.145	-1719.145022
226	1768.366	2939.249	0.184884	0.193	0.139	-1729.878966
228	1996.796	2332.747	0.205295	0.215	0.109	-1740.237210

Table 3: Tabulated results for Ra212 to Ra228 from HFBTHO v2 calculations with different Skyrme interactions. N_o represents the number of oscillator shells, β_l^* is obtained directly from the code, β_l is calculated from the multipole moments Q_l as defined in section 4.2, and B.E represents the total binding energy of the nucleus.

SLY4, $N_o = 20$						
Isotope	Q_2 (fm^2)	Q_3 (fm^3)	β_2^*	β_2	β_3	**B.E (MeV)**
212	59.338	0.000	0.007064	0.007	0.0	-1636.598238
214	3.580	0.000	0.000420	0.000	0.000	-1653.609856
216	5.920	0.000	0.000683	0.001	0.000	-1664.850360
218	921.944	1756.280	0.104063	0.107	0.090	-1676.452798
220	1224.698	2356.057	0.135365	0.140	0.118	-1688.711078
222	1445.533	2800.396	0.156669	0.163	0.138	-1700.048435
224	1647.147	3117.876	0.175160	0.183	0.151	-1710.690843
226	1850.799	3106.656	0.193326	0.202	0.147	-1720.837233
228	2037.009	2322.095	0.209520	0.220	0.108	-1730.424945
UNEDF0, $N_o = 20$						
Isotope	Q_2 (fm^2)	Q_3 (fm^3)	β_2^*	β_2	β_3	**B.E (MeV)**
212	16.365	0.000	0.001953	0.002	0.000	-1641.378739
214	4.326	0.000	0.000508	0.001	0.000	-1658.210568
216	7.429	0.001	0.000859	0.001	0.000	-1670.940753
218	800.042	1909.394	0.090438	0.093	0.097	-1683.447619
220	1130.175	2406.602	0.125066	0.129	0.121	-1695.920766
222	1373.789	2732.421	0.149014	0.155	0.134	-1707.841725
224	1571.422	2948.646	0.167258	0.174	0.142	-1719.144830
226	1767.895	2879.956	0.184840	0.193	0.137	-1729.878761
228	1994.866	2198.639	0.205120	0.215	0.103	-1740.236459
UNEDF1, $N_o = 20$						
Isotope	Q_2 (fm^2)	Q_3 (fm^3)	β_2^*	β_2	β_3	**B.E (MeV)**
212	12.062	0.000	0.001435	0.001	0.0	-1644.294624
214	4.25	0.00	0.000498	0.001	0.0	-1660.524879
216	8.547	0.000	0.000985	0.001	0.0	-1672.465875
218	830.188	1391.441	0.093666	0.096	0.071	-1683.767450
220	1183.157	2185.961	0.130618	0.135	0.109	-1696.159764
222	1424.646	2612.289	0.154145	0.161	0.128	-1707.892353
224	1633.792	2846.424	0.173426	0.181	0.138	-1718.970156
226	1840.592	2619.605	0.191954	0.201	0.124	-1729.534512
228	-	-	-	-	-	-

Table 4: Same as Table 3 but instead with HFBTHO v4.

Isotope	Half-life (Units)
Ra212	13.0 seconds
Ra213	2.73 minutes
Ra214	2.4 seconds
Ra215	1.66×10^{-3} seconds
Ra216	1.82×10^{-7} seconds
Ra217	1.6×10^{-6} seconds
Ra218	25.9×10^{-6} seconds
Ra219	9.0×10^{-3} seconds
Ra220	1.8×10^{-4} seconds
Ra221	28 seconds
Ra222	33.6 seconds
Ra223	11.4 days
Ra224	3.6 days
Ra225	14.9 days
Ra226	1.6×10^{3} years
Ra227	42.2 months
Ra228	5.75 years

Table 5: Lifetimes of Radium Isotopes. [29]

References

[1] T.E. Chupp, P. Fierlinger, M.J. Ramsey-Musolf, and J.T. Singh. "Electric dipole moments of atoms, molecules, nuclei, and particles". In: *Reviews of Modern Physics* 91.1 (Jan. 2019), p. 015001. DOI: 10.1103/RevModPhys.91.015001.

[2] N. Auerbach and V. Zelevinsky. "Nuclear structure and the search for collective enhancement of P,T -violating Schiff moments". en. In: *Journal of Physics G: Nuclear and Particle Physics* 35.9 (Sept. 2008), p. 093101. ISSN: 0954-3899, 1361-6471. DOI: 10.1088/0954-3899/35/9/093101.

[3] P. A. Butler and W. Nazarewicz. "Intrinsic reflection asymmetry in atomic nuclei". en. In: *Reviews of Modern Physics* 68.2 (Apr. 1996), 349–421. ISSN: 0034-6861, 1539-0756. DOI: 10.1103/RevModPhys.68.349.

[4] C. DeTar and T. Kunihiro. "Linear sigma model with parity doubling". en. In: *Physical Review D* 39.9 (May 1989), 2805–2808. ISSN: 0556-2821. DOI: 10.1103/PhysRevD.39.2805.

[5] R. L. Jaffe, D. Pirjol, and A. Scardicchio. "Parity Doubling Among the Baryons". en. In: 435 (Nov. 2006), 157–182. ISSN: 03701573. DOI: 10.1016/j.physrep.2006.09.004.

[6] P. A. Butler. "Studies of Heavy Pear-shaped Nuclei". en. In: *Journal of Physics: Conference Series* 2453.1 (Mar. 2023), p. 012001. ISSN: 1742-6588, 1742-6596. DOI: 10.1088/1742-6596/2453/1/012001.

[7] P. Ring and P. Schuck. *The nuclear many body problem*. eng. 1. ed., 3. print., study ed. Texts and monographs in physics. Berlin Heidelberg: Springer, 2004. ISBN: 978-3-540-21206-5.

[8] B.G. Carlsson, A. Idini, and I. Ragnarsson. *Nuclear Structure Theory: Derivation of Hartree-Fock equations from a variational approach*. http://www.matfys.lth.se/education/FMF121/HFv4.pdf. Accessed on 10-April-2024. Mathematical Physics, Lund, 2017.

[9] B.G. Carlsson, A. Idini, and I. Ragnarsson. *Nuclear Structure Theory: Introduction to the Hartree-Fock-Bogulubov method*. http://www.matfys.lth.se/education/FMF121/hfb_method.pdf. Accessed on 15-April-2024. Mathematical Physics, Lund.

[10] T. H. R. Skyrme. "The effective nuclear potential". In: *Nuclear Physics* 9.4 (Jan. 1958), 615–634. ISSN: 0029-5582. DOI: 10.1016/0029-5582(58)90345-6.

[11] J. Bartel, P. Quentin, M. Brack, C. Guet, and H. B. Håkansson. "Towards a better parametrisation of Skyrme-like effective forces: A critical study of the SkM force". In: *Nuclear Physics A* 386.1 (Sept. 1982), 79–100. ISSN: 0375-9474. DOI: 10.1016/0375-9474(82)90403-1.

[12] E. Chabanat, P. Bonche, P. Haensel, J. Meyer, and R. Schaeffer. "A Skyrme parametrization from subnuclear to neutron star densities Part II. Nuclei far from stabilities". In: *Nuclear Physics A* 635.1 (May 1998), 231–256. ISSN: 0375-9474. DOI: 10.1016/S0375-9474(98)00180-8.

[13] M. Kortelainen, T. Lesinski, J. Moré, W. Nazarewicz, J. Sarich, N. Schunck, M. V. Stoitsov, and S. Wild. "Nuclear energy density optimization". en. In: *Physical Review C* 82.2 (Aug. 2010), p. 024313. ISSN: 0556-2813, 1089-490X. DOI: 10.1103/PhysRevC.82.024313.

[14] M. Kortelainen, J. McDonnell, W. Nazarewicz, P.-G. Reinhard, J. Sarich, N. Schunck, M. V. Stoitsov, and S. M. Wild. "Nuclear energy density optimization: Large deformations". en. In: *Physical Review C* 85.2 (Feb. 2012), p. 024304. ISSN: 0556-2813, 1089-490X. DOI: 10.1103/PhysRevC.85.024304.

[15] R. W. Hasse and W. D. Myers. *Geometrical relationships of macroscopic nuclear physics*. Springer series in nuclear and particle physics. Berlin; New York: Springer-Verlag, 1988. ISBN: 978-0-387-17510-2.

[16] S.G. Nilsson. "Binding states of individual nucleons in strongly deformed nuclei". In: *Dan. Mat. Fys. Medd.* 29.CERN-55-30 (1955), pp. 1–69.

[17] A.N. Bohr and B.R. Mottelson. "Collective and individual-particle aspects of nuclear structure". In: *Dan. mat. fys. Medd.* 27.CERN-57-38 (1953), pp. 1–174.

[18] M. V. Stoitsov, N. Schunck, M. Kortelainen, N. Michel, H. Nam, E. Olsen, J. Sarich, and S. Wild. "Axially deformed solution of the Skyrme-Hartree-Fock-Bogolyubov equations using the transformed harmonic oscillator basis (II) HFBTHO v2.00d: a new version of the program". In: *Computer Physics Communications* 184.6 (June 2013). arXiv:1210.1825 [nucl-th], 1592–1604. ISSN: 00104655. DOI: 10.1016/j.cpc.2013.01.013.

[19] P. Marevic, N. Schunck, E. M. Ney, R. Navarro Pérez, M. Verriere, and J. O'Neal. "Axially-deformed solution of the Skyrme-Hartree-Fock-Bogoliubov equations using the transformed harmonic oscillator basis (IV) hfbtho (v4.0): A new version of the program". In: *Computer Physics Communications* 276 (July 2022). arXiv:2110.06424 [nucl-th], p. 108367. ISSN: 00104655. DOI: 10.1016/j.cpc.2022.108367.

[20] P. Reinhard, Bastian Schuetrumpf, and J.A. Maruhn. "The Axial Hartree–Fock + BCS Code SkyAx". In: *Computer Physics Communications* 258 (Jan. 2021), p. 107603. DOI: 10.1016/j.cpc.2020.107603.

[21] P.A. Butler, L.P. Gaffney, P. Spagnoletti, K. Abrahams, M. Bowry, J. Cederkäll, G. De Angelis, H. De Witte, P.E. Garrett, A. Goldkuhle, C. Henrich, A. Illana, K. Johnston, D.T. Joss, J.M. Keatings, N.A. Kelly, M. Komorowska, J. Konki, T. Kröll, M. Lozano, B.S. Nara Singh, D. O'Donnell, J. Ojala, R.D. Page, L.G. Pedersen, C. Raison, P. Reiter, J.A. Rodriguez, D. Rosiak, S. Rothe, M. Scheck, M. Seidlitz, T.M. Shneidman, B. Siebeck, J. Sinclair, J.F. Smith, M. Stryjczyk, P. Van Duppen, S. Vinals, V. Virtanen, N. Warr, K. Wrzosek-Lipska, and M. Zielińska. "Evolution of Octupole Deformation in Radium Nuclei from Coulomb Excitation of Radioactive Ra 222 and Ra 228 Beams". en. In: *Physical Review Letters* 124.4 (Jan. 2020), p. 042503. ISSN: 0031-9007, 1079-7114. DOI: 10.1103/PhysRevLett.124.042503.

[22] Y. Cao, S. E. Agbemava, A. V. Afanasjev, W. Nazarewicz, and E. Olsen. "Landscape of pear-shaped even-even nuclei". In: *Physical Review C* 102.2 (Aug. 2020). arXiv:2004.01319 [nucl-th], p. 024311. ISSN: 2469-9985, 2469-9993. DOI: 10.1103/PhysRevC.102.024311.

[23] B. E. Chi. "Single-particle energy levels in a Nilsson well". In: *Nuclear Physics* 83.1 (July 1966), 97–144. ISSN: 0029-5582. DOI: 10.1016/0029-5582(66)90344-0.

[24] V. I. Kuprikov and V. N. Tarasov. "Study of Octupole Deformation of Radium Isotopes in the Hartree–Fock–Bogoliubov Approximation with Skyrme Forces: Physics of Atomic Nuclei". In: *Physics of Atomic Nuclei* 84.6 (Nov. 2021), 796–803. ISSN: 10637788. DOI: 10.1134/S1063778821050094.

[25] H. J. Lipkin. "Collective motion in many-particle systems: Part 1. The violation of conservation laws". In: *Annals of Physics* 9.2 (Feb. 1960), 272–291. ISSN: 0003-4916. DOI: 10.1016/0003-4916(60)90032-4.

[26] J. Dobaczewski. "Lipkin translational-symmetry restoration in the mean-field and energy–density-functional methods". en. In: *Journal of Physics G: Nuclear and Particle Physics* 36.10 (Sept. 2009), p. 105105. ISSN: 0954-3899. DOI: 10.1088/0954-3899/36/10/105105.

[27] P. Moller, A. J. Sierk, T. Ichikawa, and H. Sagawa. "Nuclear ground-state masses and deformations: FRDM(2012)". In: *Atomic Data and Nuclear Data Tables* 109–110 (May 2016). arXiv:1508.06294 [nucl-th], 1–204. ISSN: 0092640X. DOI: 10.1016/j.adt.2015.10.002.

[28] P. A. Butler. "Octupole collectivity in nuclei". en. In: *Journal of Physics G: Nuclear and Particle Physics* 43.7 (July 2016), p. 073002. ISSN: 0954-3899, 1361-6471. DOI: 10.1088/0954-3899/43/7/073002.

[29] *NuDat 3.0 Database*. https://www.nndc.bnl.gov/nudat3. Accessed on 10-May-2024.

[30] A. Såmark-Roth, L. G. Sarmiento, D. Rudolph, J. Ljungberg, M. Carlsson, C. Fahlander, U. Forsberg, P. Golubev, I. Ragnarsson, D. Ackermann, and et al. "Low-lying states in Ra219 and Rn215: Sampling microsecond -decaying nuclei". en. In: *Physical Review C* 98 (2018), p. 044307. ISSN: 2469-9985. DOI: 10.1103/physrevc.98.044307.

[31] *KAERI Database*. https://atom.kaeri.re.kr. Accessed on 26-June-2024.